

Manifold formation and crossings of ultracold lattice spinor atoms in the intermediate interaction regime

Xue-Ting Fang, Zheng-Qi Dai , Di Xiang, Shou-Long Chen, Shao-Jun Li, Xiang Gao, Qian-Ru Zhu, Xing Deng, Lushuai Cao,^{*} and Zhong-Kun Hu

MOE Key Laboratory of Fundamental Physical Quantities Measurement and Hubei Key Laboratory of Gravitation and Quantum Physics, PGMF and School of Physics, Huazhong University of Science and Technology, Wuhan 430074, People's Republic of China

 (Received 30 May 2022; revised 9 August 2022; accepted 1 September 2022; published 16 September 2022)

Ultracold spinor atoms in the weak and strong interaction regimes have been extensively investigated, while the behavior in the intermediate regime is less understood. We numerically investigate one-dimensional ultracold spinor atomic ensembles of finite size in the intermediate interaction regime and reveal the evolution of the eigenstates from the strong to the intermediate regime. In the strong interaction regime, it is well known that the eigenstates can be categorized into different manifolds, and the categorization is protected by the energy gaps between manifolds. In the intermediate interaction regime, it is found that the eigenenergy spectrum becomes gapless, while categorization of the eigenstates is still preserved even without the protection from the intermanifold gaps. The categorization in the intermediate regime is found due to the minigap induced by the finite-size effect, which prevents the intermanifold coupling. The gap vanishing in the spectrum induces both direct and avoided crossings between close-lying manifolds, of which the combined symmetries determine the type of the crossings. A modified t - J model is derived to describe the low-lying eigenstates in the intermediate regime, which can capture the formation and crossings of the manifolds. State preparation through avoided crossings is also investigated.

DOI: [10.1103/PhysRevA.106.033315](https://doi.org/10.1103/PhysRevA.106.033315)

I. INTRODUCTION

Spinor quantum gases normally refer to ultracold atoms, the internal states of which are taken as the spin degree of freedom [1,2]. Ultracold spinor gases have become an important platform in various fields, such as quantum magnetism, the quantum phase transition, and topological excitations. Magnetic phases [3–6] and associated phase transitions [7–15] have been investigated on the spinor atomic platform, and various topological excitations such as vortices [16–18] and monopoles [19–21] have also been theoretically proposed and experimentally realized with spinor atoms. Besides the fundamental interests, spinor atoms also provide a promising platform for quantum simulations [22–29] and quantum metrology [30–34]. Simulations of, e.g., topological systems [27–29] and high-energy physics [22–25] have been realized with lattice spinor atoms. Entangled and/or squeezed spinor atoms [35–37] are well recognized as important sources in quantum measurements.

The interaction between spinor atoms plays a key role in the above-mentioned studies and applications. Theoretical tools have been developed for spinor atoms in the weak and strong interaction regimes and have provided deep insights into the stationary and dynamical behaviors in the corresponding interaction regimes. In the weak interaction regime, the spinor atoms are in the condensate state and are well described by the single-mode approximation (SMA), in which the condensate state is assumed to take the same spatial

wave function for all spin states. The ground state [38–50], excitation [42–44,51], and dynamical properties [45,52–54] of the spinor condensate have been revealed using the SMA, and the validity of the SMA has also been investigated [42,54]. In the Tonks-Girardeau (TG) regime [55–58], Bose-Fermi mapping is a good analytical tool for spinor atoms. In the strong interaction regime, an analytical ansatz based on perturbation treatment with Bose-Fermi mapping has been developed and provided good understanding of the half-spin [59–69] and integer-spin [70–72] systems, which revealed the multimaniifold structure in the eigenenergy spectrum and the effective Heisenberg model for each manifold. Strongly interacting spinor atoms have become a promising test bed for the strong-correlation-induced phase [61–63,72] transition and dynamical processes [59,67].

Between the weak and strong interaction regimes, there lies a wide intermediate regime, in which the behavior of the spinor atoms is less well understood. Concerning the lattice spinor atoms, the transition between the three interaction regimes can be indicated by two criteria, namely, the appearance of gaps in the eigenenergy spectrum and the local-density fluctuation in the lattice. The weak interaction regime is characterized by the gapless spectrum and large occupation fluctuation, whereas in the strong interaction regime the spectrum becomes well gapped and the occupation fluctuation is strongly suppressed in the low-lying eigenstates. The intermediate regime behaves as a hybrid of the weak and strong interaction regimes, with the gapless spectrum and the suppressed local occupation fluctuation. This hybridization suggests that the intermediate regime could provide novel phenomena different from those in the weak and strong in-

^{*}lushuai_cao@hust.edu.cn

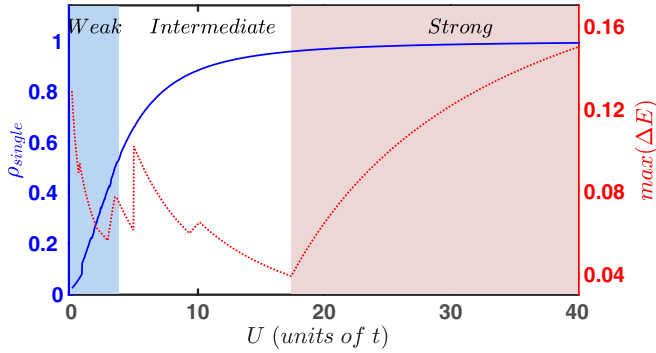


FIG. 1. Sketch of the transition between the weak, intermediate, and strong interaction regimes in terms of the appearance of the energy gap (red) and the total probability of the single-occupation basis states (blue). The results are calculated with the finite ($3 \uparrow 3 \downarrow 1h$) system.

teraction regimes. In the intermediate and strong interaction regimes, the suppression of the local occupation fluctuation in the low-lying eigenstates is attributed to the dominance of the single-occupation basis states in these eigenstates, which refers to states with local occupation of each site no bigger than one. Figure 1 sketches the transition between the three interaction regimes, in which the energy gaps and the density fluctuation are illustrated by the maximum energy difference between close-lying eigenstates $\max(\Delta E)$ and the probability of single-occupation states ρ_{single} , respectively. The total probability of the single-occupation basis in the intermediate and strong interaction regimes grows more than one half, indicating the dominant role of the basis in these regimes and the suppression of local-density fluctuation due to the higher-occupation basis states. Here $\max(\Delta E)$ presents a fluctuating and monotonic increasing behavior below and within the strong interaction regime, respectively. The monotonic increase indicates the arising of the energy gap in the spectrum, which increases with the interaction strength. The fluctuation in the weak and intermediate regimes is actually due to the finite-size effect, which introduces minigaps between close-lying eigenstates. In the limit of infinite long lattice, the minigaps will vanish, and the spectrum will become exactly gapless.

In this work, we perform numerical simulations on finite ultracold spinor atoms confined in a one-dimensional optical lattice, and our numerical simulation reveals the transition from the strong to the intermediate regime. It is been known that in the strong interaction regime, the eigenenergy spectrum presents a well-gapped multimanifold structure, and the eigenstates can be correspondingly categorized into different manifolds [60,65], which are protected by the energy gaps against intermanifold coupling. In the intermediate regime, the energy spectrum becomes gapless, implying that the categorization would fail in this regime. However, our simulation reveals that the eigenstates can still be categorized into different manifolds, even without the protection of the energy gap between different manifolds. It turns out that the categorizability of the eigenstates in the intermediate regime is attributed to the minigaps induced by the finite-size effect, which refers to the finite energy spacing between close-lying

eigenstates. The minigaps dominate over the intermanifold coupling and maintain the categorization of the eigenstates. The gapless energy spectrum gives rise to the overlapping and rich energy-level crossings between different manifolds, including direct and avoided crossings. The avoided crossings can be explored for state preparation and manipulation. We derived a modified t - J model to describe the lattice spinor atoms in the intermediate regime, and the t - J model well explains the manifold structure preservation in the intermediate regime and reveals the influence of the spin and spatially related symmetries on determining whether the energy-level crossing is a direct or avoided one. The dynamical magnetization through the interaction quench between avoided crossing points is also numerically demonstrated.

This paper is organized as follows: In Sec. II we present the setup under consideration and present the derivation of our low-energy effective Hamiltonians. In Sec. III we show the energy spectrum obtained from the numerical method and energy-level crossings between different manifolds. Finally, a brief discussion and conclusion are given in Sec. IV.

II. SETUP AND EFFECTIVE HAMILTONIANS

We consider bosonic spinor atoms confined in one-dimensional optical lattices. The effective spin degree of freedom is spanned by the internal states of the atoms, e.g., the hyperfine ground states $|F = 2, m_F = 0\rangle$ and $|F = 3, m_F = 0\rangle$ for ^{87}Rb atoms, and are denoted as $|\uparrow\rangle$ and $|\downarrow\rangle$; that is to say, we focus on the effective spin-1/2 atomic systems in this work. The lattice spinor atomic system is subjected to the Bose-Hubbard Hamiltonian:

$$H = -t \sum_{\langle i,j \rangle} \sum_{\sigma=\uparrow,\downarrow} \hat{a}_{i,\sigma}^\dagger \hat{a}_{j,\sigma} + U \sum_{i=1}^{2N+1} \sum_{\sigma,\sigma'=\uparrow,\downarrow} \hat{a}_{i,\sigma}^\dagger \hat{a}_{i,\sigma'}^\dagger \hat{a}_{i,\sigma'} \hat{a}_{i,\sigma}, \quad (1)$$

where $\hat{a}_{i,\sigma}$ ($\hat{a}_{i,\sigma}^\dagger$) indicates the annihilation (creation) operators of an atom of spin state σ in the i th site. $\langle i, j \rangle$ denotes the summation over the nearest neighbors in the lattice. We consider the optical lattice with the open boundary condition, and the first and second terms of H refer to the nearest-neighbor hopping and the on-site interaction of the atoms, respectively, where t and U are the spin-independent tunneling strength and contact interaction strength.

The numerical simulations are performed on finite spin-balanced atomic ensembles with N spin-up and N spin-down atoms confined in a lattice with $2N + 1$ sites, i.e., the case of single-hole filling. The eigenstates of the system are obtained by exact diagonalization using the multilayer multiconfiguration time-dependent Hartree method for mixtures of arbitrary species (ML-MCTDHF) [73–75], in which no truncation to the Hilbert space is applied, and the full configuration-interaction calculations are performed. Given that the low-lying eigenstates we are concerned with in this work are dominated by the single-occupation basis states, our analysis of the numerical results focuses on the truncated Hilbert space spanned by the single-occupation states, which manifest as the direct product of the charge sector and spin sector. The charge sector is spanned by the configuration space of a single hole hopping in the $(2N + 1)$ -site lattice, and the spin sector corresponds to a spin chain of

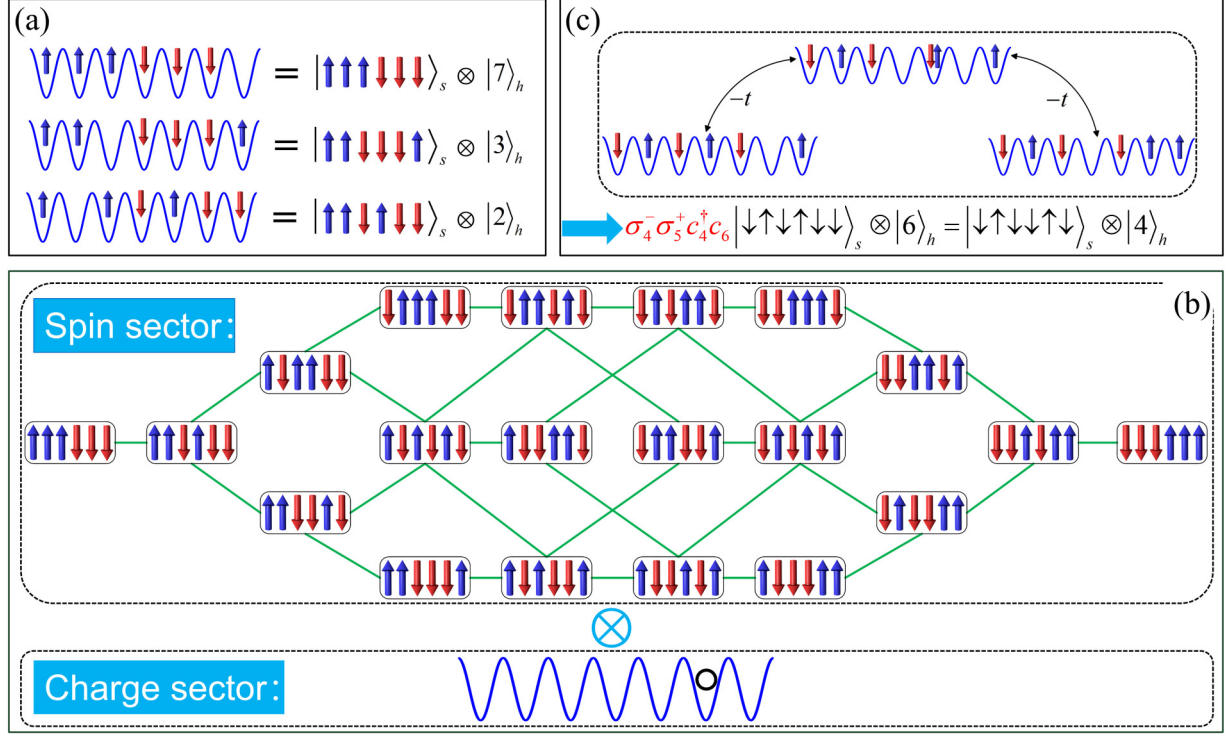


FIG. 2. Illustration of spin-charge separation in the $(3 \uparrow 3 \downarrow 1h)$ system: (a) basis transformation from the original to the spin-charge basis, (b) the configuration space of the spin and charge sectors, and (c) the high-order tunneling process of the simultaneous spin flipping and next-nearest-neighbor hopping of the hole via the intermediate double-occupation states.

$2N$ spins in the squeezed space, with the hole removed from the lattice [76,77]. This leads to the transformation of the single-occupation states to the product form as

$$\hat{a}_{i_1, \sigma_1}^\dagger \hat{a}_{i_2, \sigma_2}^\dagger \cdots \hat{a}_{i_{2N}, \sigma_{2N}}^\dagger |\text{Vac}\rangle = |i\rangle_H \otimes |\sigma_1 \sigma_2 \cdots \sigma_{2N}\rangle_S, \quad (2)$$

with $i_1 < i_2 < \cdots < i_{2N}$ and $|\text{Vac}\rangle$ referring to the vacuum state of the lattice. $|i\rangle_H$ is the basis state in the charge sector and indicates the location of the hole in the lattice. $|\sigma_1 \sigma_2 \cdots \sigma_{2N}\rangle_S$ denotes the Fock configuration of the spin chain in the spin sector. Figure 2(a) illustrates the transformation of the single-occupation states to the direct product form in the finite system of three spin-up atoms and three spin-down atoms confined in a lattice of seven sites, denoted as $(3 \uparrow 3 \downarrow 1h)$ in the following. Figure 2(b) sketches the configuration space constituted of the spin and charge sectors of the $(3 \uparrow 3 \downarrow 1h)$ system.

Following the decomposition of the truncated Hilbert space to the spin and charge sectors, the Bose-Hubbard Hamiltonian is transformed to the modified t - J model [78–81]. The modified t - J model of single-hole filling systems reads

$$H_{t-J} = H_{\text{hole}} + H_{\text{spin}}, \quad (3a)$$

$$H_{\text{hole}} = -t \sum_{i=1}^{2N} (\hat{c}_i^\dagger \hat{c}_{i+1} + \text{H.c.}), \quad (3b)$$

$$H_{\text{spin}} = -J \sum_{i=1}^{N-1} (\vec{\sigma}_i \cdot \vec{\sigma}_{i+1} + 3) \left(1 - \frac{\hat{c}_{i+1}^\dagger \hat{c}_{i+1} + \hat{c}_i^\dagger \hat{c}_i + 2}{2} \right), \quad (3c)$$

where $c_i^{(\dagger)}$ refers to the annihilation (creation) operator of the hole in the i th site of the lattice and $\vec{\sigma}_j \equiv (\sigma_j^x, \sigma_j^y, \sigma_j^z)$ is the Pauli matrices of the j th spin in the squeezed space. H_{hole} describes the hopping of the hole in the charge sector, and H_{spin} in the spin sector indicates the spinor atoms in the squeezed space organized to the Heisenberg spin chain. It is worth noticing that in H_{spin} the spin-spin interaction strength in the spin sector is dependent on the local occupation and next-nearest-neighbor correlations of the hole in the charge sector, which gives rise to the coupling between the charge and spin sectors. The coupling between the two sectors is attributed to the second-order tunneling process, with $J = t^2/U$. Figure 2(c) sketches the action of simultaneous spin flipping and next-nearest-neighbor hopping of the hole in H_{spin} , which is mediated by double-occupation states. A more detailed demonstration of the derivation and validity of the effective t - J Hamiltonian is given in Appendix A.

Under the condition of $J \ll t$, which is valid in the intermediate and strong interaction regimes, H_{t-J} is dominated by H_{hole} , and it is convenient to transform the basis states in the charge sector from the hole-occupation state to the eigenstates of H_{hole} , which will more clearly illustrate the manifold formation and crossings. Under this transformation, H_{t-J} can be reformed as $H_{t-J} = H_{\text{manfd}} + H_{\text{scatt}}$, with

$$H_{\text{manfd}} = \sum_{\alpha=1}^{2N+1} |w_\alpha\rangle_H \langle w_\alpha| \left(\varepsilon_\alpha - J \sum_{i=1}^{N-1} W_i^\alpha \vec{\sigma}_i \vec{\sigma}_{i+1} \right), \quad (4a)$$

$$H_{\text{scatt}} = \frac{J}{2} \sum_{\alpha_1 \neq \alpha_2}^{2N+1} |w_{\alpha_1}\rangle_H \langle w_{\alpha_2}| \left(\sum_{i=1}^{N-1} W_i^{\alpha_1, \alpha_2} \vec{\sigma}_i \vec{\sigma}_{i+1} \right). \quad (4b)$$

In the above equations, $|w_\alpha\rangle_H$ refers to the α th eigenstate of H_{hole} , with $w_\alpha(i)$ and ϵ_α denoting the corresponding eigenwave function and eigenenergy, respectively. The coefficients W_i^α and $W_i^{\alpha_1, \alpha_2}$ are defined as $W_i^\alpha = [1 - |w_\alpha(i)|^2 + w_\alpha^*(i)w_\alpha(i+2)]$ and $W_i^{\alpha_1, \alpha_2} = [2w_{\alpha_1}^*(i)w_{\alpha_2}(i) - w_{\alpha_1}^*(i)w_{\alpha_2}(i+2) - w_{\alpha_2}^*(i)w_{\alpha_1}(i+2)]$. H_{manfd} is the leading term of H_{t-J} , in which the hole remains in the same eigenstates of H_{hole} , and the spin sector turns to the Heisenberg spin chain, with the spin-spin interaction dependent on the state of the hole, which is consistent with the derivation of the site-dependent spin-spin interaction in [60,65,66]. H_{scatt} describes the scattering between different $|w_\alpha\rangle_H$ in the charge sector, with the spin sector maintaining the Heisenberg spin chain.

In the strong interaction regime, the energy difference between $|w_\alpha\rangle_H$ is much stronger than the scattering strength of H_{scatt} , which prevents the coupling between different $|w_\alpha\rangle_H$. The eigenstates of H_{manfd} , that is, $|\alpha, \Sigma\rangle \equiv |w_\alpha\rangle_H \otimes |\Sigma(\alpha)\rangle_S$, represent a good approximation of those of H_{t-J} , in which $|\Sigma(\alpha)\rangle_S$ refers to the eigenstates of the Heisenberg chain in the spin sector. $|\alpha, \Sigma\rangle$ can be categorized into different manifolds with respect to $|w_\alpha\rangle_H$, and in the eigenenergy spectrum of H_{t-J} , eigenstates of the same manifold are well localized around the corresponding ϵ_α , which leads to the well-known multimaniifold structure in the low-lying eigenenergy spectrum in the strong interaction regime of H_{t-J} . In summary, the categorization of the eigenstates of H_{t-J} with respect to $|w_\alpha\rangle_H$ in the strong interaction regime is protected by the energy gaps between different $|w_\alpha\rangle_H$, which prevents the coupling between different $|w_\alpha\rangle_H$.

In the intermediate interaction regime, however, the coupling between different manifolds due to H_{scatt} becomes stronger and cannot be neglected, which affects the categorization of the low-lying eigenstates. Before proceeding to the details in the intermediate regime, it is worth paying attention to the symmetries in H_{manfd} and H_{scatt} , which play an important role in the coupling between different manifolds. In H_{manfd} , the charge sector is subjected to the space-reflection symmetry \hat{T}_{rc} , and the spin sector is subjected to both the space-reflection symmetry \hat{T}_{rs} and the spin-flipping symmetry \hat{T}_{fs} . Each $|\alpha, \Sigma\rangle$ is associated with three parities (T_{rc}, T_{rs}, T_{fs}), which correspond to the parities of the space-reflection symmetry in the charge and spin sectors and that of the spin-flipping symmetry, with $T_{rc}, T_{rs}, T_{fs} \in \{\pm\}$. The Hamiltonian H_{scatt} , however, is invariant under the action of \hat{T}_{fs} and $\hat{T}_{rc}\hat{T}_{rs}$ but not the individual action of \hat{T}_{rc} or \hat{T}_{rs} . The different symmetries of H_{manfd} and H_{scatt} lead to H_{scatt} being able to couple only $|\alpha, \Sigma\rangle$ with the same parity (product) for T_{fs} and $T_{rc}T_{rs}$.

III. NUMERICAL RESULTS FOR THE MANIFOLD FORMATION AND CROSSINGS

We present the numerical results for the eigenenergy spectrum of the $(3 \uparrow 3 \downarrow 1h)$ system in Fig. 3(a). The calculations are carried out based on the Bose-Hubbard Hamiltonian H in the complete Hilbert space, while only the low-lying eigenenergy spectrum dominated by the single-occupation states is shown. The eigenenergy spectrum is calculated with the interaction strength U scanned over a wide interval from the weak regime to approaching the TG regime, where the eigen-

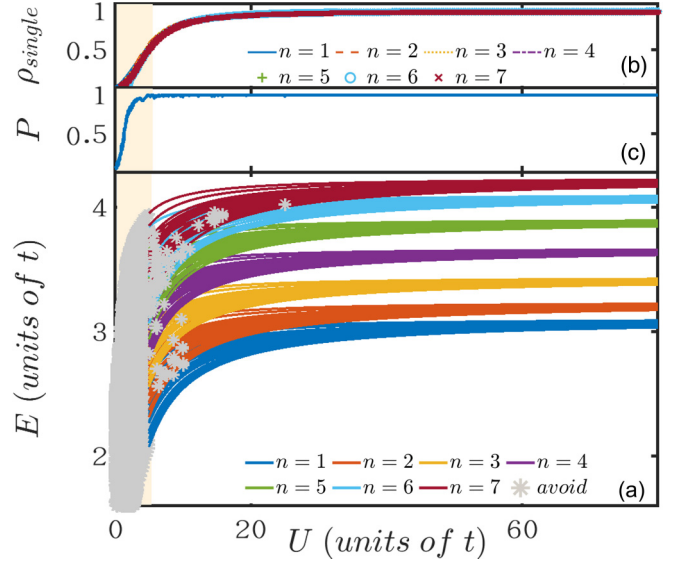


FIG. 3. (a) The eigenenergy spectrum for $(3 \uparrow 3 \downarrow 1h)$. Eigenstates of the same manifold are marked with the same color, and the eigenenergy of uncategorized eigenstates is shown with gray stars. (b) The probability of the single-occupation basis of the eigenstates in each manifold; the lowest probability of all the eigenstates in each manifold is plotted. (c) The ratio of categorizable eigenstates to the total low-lying eigenstates in different interaction regimes.

ergy spectrum saturates to the fermionization limit. In the strong interaction regime with the well-gapped multimaniifold structure, the eigenstates can be categorized into different manifolds, and eigenstates in the same manifold are well approximated by $|\alpha, \Sigma\rangle$ with the same α . The multimaniifold structure is protected by the energy gaps, which prevent intermanifold coupling induced by H_{scatt} . As the interaction decreases from the strong interaction regime, the gaps vanish in the spectrum, which marks the transition from the strong to the intermediate regime. On the other side of the spectrum, the transition between the intermediate and weak interaction regimes is captured by the decrease of the total probability of the single-occupation basis as U decreases, as shown in Fig. 3(b).

In the intermediate interaction regime, where the energy gaps vanish between close-lying manifolds in the spectrum, an immediate question is whether the eigenstates can still be categorized into different manifolds with no protection of the energy gaps against the intermanifold coupling. To directly address this question, we apply the wave-function categorization to eigenstates in the intermediate regime, and wave-function categorization is based on the wave-function identification through supervised machine learning [82–84], which adapts the procedure in Refs. [85,86]. In the supervised categorization, the training set is chosen from the eigenstates in the strong interaction regime, with each eigenstate labeled by the manifold it belongs to, and the trained network is used to categorize the eigenstates in the whole interaction interval in Fig. 3(a). More details on the setting of the machine learning procedure are given in Appendix B.

The categorization results are illustrated by different colors in Fig. 3(a): The eigenenergies marked with the same color

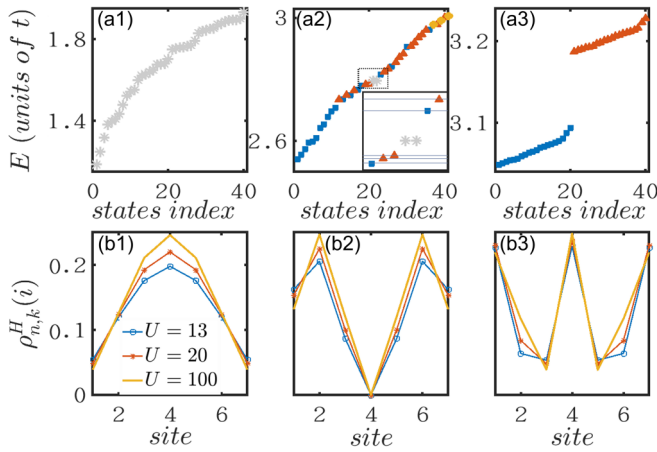


FIG. 4. Eigenenergy spectrum for (a1) $U = 1.6$, (a2) $U = 10$, and (a3) $U = 65$; the gray stars refer to the uncategorizable eigenstates, and the blue squares, red triangles, and yellow dots indicate the eigenstates recognized as belonging to the first, second, and third manifolds, respectively. The inset of (a2) zooms in on the area marked by the dashed box in the main panel, in which the bars located at each categorizable eigenenergy point measure the intermanifold coupling. (b1)–(b3) The spatial distribution of the hole for eigenstates in the first, second, and third manifolds, respectively, at $U = 13$, $U = 20$, and $U = 100$.

indicate the corresponding eigenstates belong to the same manifold. The eigenenergies marked by gray stars indicate the supervised categorization failed for the corresponding eigenstates with a predicted score below 0.95. It is found that in the weak interaction regime, all eigenenergies are marked in gray, indicating that the eigenstates in this regime cannot be categorized into different manifolds. In the intermediate regime, however, most eigenenergies are well colored, and this indicates that in the intermediate regime most eigenstates can still be categorized into different manifolds, even without the explicit gaps between close-lying manifolds. It is also noticeable that a few exceptional uncategorizable eigenstates arise in the intermediate regime, which are marked by the sparse gray stars immersed in the well-colored spectrum in this regime. Figure 3(c) quantifies the categorizability in terms of the ratio of categorizable eigenstates to the total low-lying eigenstates in different interaction regimes. In the intermediate regime, the ratio is as high as almost unity, indicating that most eigenstates can be categorized into different manifolds in this regime. In the weak interaction regime, the ratio presents a relatively sharp decrease to zero, and the categorization completely fails. Figure 3(c) suggests that the categorizability is consistent with the transition between the weak and intermediate interaction regimes.

Figures 4(a1)–4(a3) provide a close look at the eigenenergy spectra in the weak, intermediate, and strong interaction regimes, respectively, in which the first 40 eigenenergies are shown, with the color indicating the categorization as in Fig. 3(a). In the weak interaction regime, as shown in Fig. 4(a1), the spectrum is gapless, and the eigenenergies are marked in gray, indicating that the corresponding eigenstates cannot be categorized. In contrast, in the strong interaction regime, the spectrum plotted in Fig. 4(a3) is well gapped,

which protects the categorization and the multimaniifold structure. In Fig. 4(a2), the spectrum in the intermediate regime becomes gapless, whereas most eigenstates are still categorizable and grouped into different manifolds. The vanishing of the energy gap leads to the overlap of different manifolds in the spectrum.

Figures 4(b1)–4(b3) plot the spatial distribution of the hole for eigenstates in the first three manifolds at different interaction strengths in the strong and intermediate regimes. The spatial distribution is defined as $\rho_{n,k}^H(i) = \langle n, k | \hat{c}_i^\dagger \hat{c}_i | n, k \rangle$, with $|n, k\rangle$ indicating the k th eigenstates in the n th manifolds. It is shown that $\rho_{n,k}^H$ of a given manifold remains qualitatively the same as the interaction changes from the strong to the intermediate regime. Moreover, $\rho_{n,k}^H$ with $n = 1, 2, 3$ resemble the density distribution of $|w_\alpha\rangle_H$ with $\alpha = 1, 2, 3$, respectively, which indicates the projection of the corresponding eigenstates in the charge sector dominated by $|w_\alpha\rangle_H$. This demonstrates that each categorizable eigenstate can be approximated by $|\alpha, \Sigma\rangle$ in both the strong and intermediate regimes.

In order to illustrate how the categorization is maintained in the intermediate regime, we zoom in on the area around a pair of gray eigenenergies in the main panel in Fig. 4(a2) and compare the categorizable and uncategorizable eigenenergies in the inset. It can be seen that the categorizable eigenstates are separated by a nonvanishing energy spacing induced by the finite-size effect, while the uncategorizable pair is almost degenerate. For the categorizable eigenstates, which are well approximated by $|\alpha, \Sigma\rangle$, the H_{scatt} -induced intermanifold coupling is calculated and illustrated by the width of the shaded bar located at the associated eigenenergies. It can be seen that the energy spacing between the categorizable eigenenergies is much wider than the width of the shaded bars, which demonstrates that the nonvanishing energy spacing prevents the intermanifold coupling and maintains the formation of the manifold structure.

The major difference between the intermediate and strong interaction regimes lies in the uncategorizable eigenstates, which arise from the accidental degeneracy between $|\alpha, \Sigma\rangle$ with different α . The accidental degeneracy also manifests as the crossing between different energy levels in the spectrum. Figure 5(a1) takes the crossings between $|n = 7, k = 6\rangle$ and $|n = 6, k = 16, 17, 18, 19\rangle$, for example, where two types of crossings arise: One type of crossing is associated with the appearance of uncategorized eigenstates, indicated by the crossings between $|n = 7, k = 6\rangle$ and $|n = 6, k = 16, 19\rangle$, and the other is not, as exemplified by the crossings between $|n = 7, k = 6\rangle$ and $|n = 6, k = 17, 18\rangle$. Figure 5(a2) zooms in on the crossing between $|n = 7, k = 6\rangle$ and $|n = 6, k = 16\rangle$ and illustrates that the crossing point associated with the uncategorized eigenstates manifests as the avoided crossing. The crossings with no uncategorized eigenstates are then direct crossings. The coexistence of the two types of crossings is attributed to the symmetry constraints on H_{scatt} as discussed in the previous section, of which H_{scatt} can couple only $|n, k\rangle$ with the same parities of \hat{T}_{fs} and $\hat{T}_{rc}\hat{T}_{rs}$. In Fig. 5(a2), $|n = 6, k = 17\rangle$ and $|n = 6, k = 18\rangle$ break the constraint on \hat{T}_{fs} and $\hat{T}_{rc}\hat{T}_{rs}$ with $|n = 7, k = 6\rangle$, respectively, and direct crossing between these eigenstates is observed.

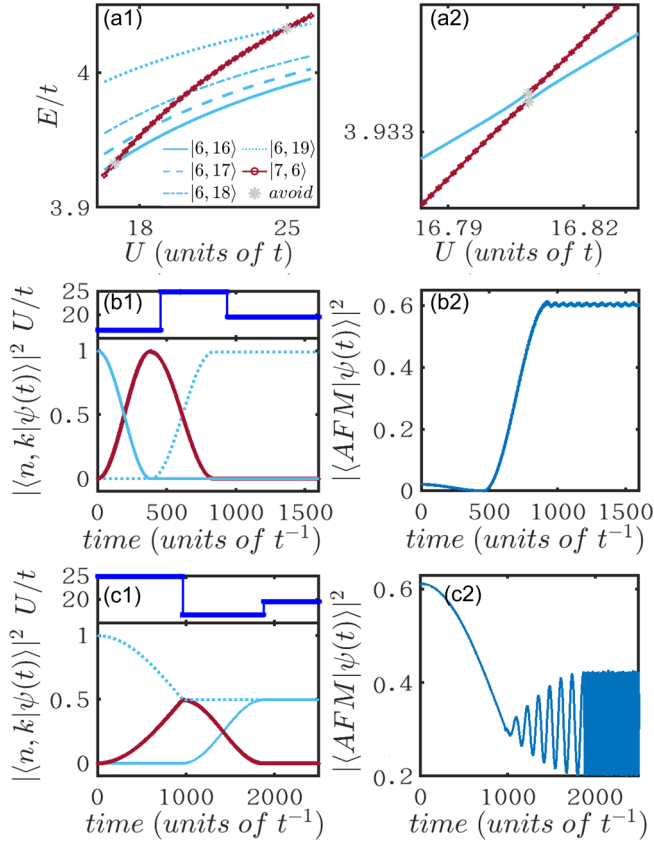


FIG. 5. (a1) Eigenenergy as a function of the interaction strength for $|n=6, k=16, 17, 18, 19\rangle$ and $|n=7, k=6\rangle$, around their crossings. The gray stars mark the uncategorized eigenenergies. (a2) Zoom of the crossing between $|n=6, k=16\rangle$ and $|n=7, k=6\rangle$. Eigenstate transfer from $|n=6, k=19\rangle$ to $|n=6, k=16\rangle$ through two-step interaction quenches, with (b1) the probability of the corresponding eigenstates and (b2) the probability of the AFM state. The top panel in (b1) shows the interaction quench sequence. Eigenstate transfer from $|n=6, k=19\rangle$ to the superposition of $|n=6, k=16\rangle$ and $|n=6, k=19\rangle$ through two-step interaction quenches, with (c1) the probability of the corresponding eigenstates and (c2) the probability of the AFM state. The top panel in (c1) shows the interaction quench sequence.

The avoided crossing between a pair of $|n, k\rangle$ can induce the Rabi-like oscillation between the corresponding eigenstates and can be explored for state preparations through interaction quenches. Initializing the system in $|n=6, k=16\rangle$, we demonstrate in Figs. 5(b) and 5(c) that the system can be transferred to $|n=6, k=19\rangle$ and the superposition of $|n=6, k=16\rangle$ and $|n=6, k=19\rangle$ as a function of time, respectively. The state transfer is accomplished through a two-step interaction quench, mediated by $|n=7, k=6\rangle$. Figure 5(b1) shows that the system is initially prepared in $|n=6, k=16\rangle$, and when the interaction is quenched to the bottom avoided-crossing point in Fig. 5(a1), the system evolves to $|n=7, k=6\rangle$. Once the system is completely transferred to $|n=7, k=6\rangle$, the interaction is quenched to the upper avoided crossing, which finally transfers the system to $|n=6, k=19\rangle$. At each avoided-crossing point, the system undergoes a half-period

Rabi-like oscillation between the corresponding eigenstates. Given that the projection of $|n=6, k=19\rangle$ in the spin sector is dominated by the antiferromagnetic (AFM) state $|S_{\text{AFM}}\rangle = (|\uparrow\uparrow\downarrow\downarrow\rangle + |\downarrow\downarrow\uparrow\uparrow\rangle)/\sqrt{2}$, this two-step quench can be used for antiferromagnetic state preparation. Similarly, in Fig. 5(c1), the system can be prepared in the superposition of $|n=6, k=16\rangle$ and $|n=6, k=19\rangle$ through a two-step interaction quench, where the first quench induces a quarter-period oscillation between $|n=7, k=6\rangle$ and $|n=6, k=19\rangle$ and transfers the system to the superposition of the two eigenstates. The second quench further transfers the system to the superposition of $|n=6, k=16\rangle$ and $|n=6, k=19\rangle$ by a half-period oscillation between $|n=6, k=16\rangle$ and $|n=7, k=6\rangle$. This series of quenches leads to a quantum beating between the antiferromagnetic state and the bispinon state $|S_{\text{BP}}\rangle = (|\uparrow\downarrow\downarrow\uparrow\rangle + |\downarrow\uparrow\uparrow\downarrow\rangle)/\sqrt{2}$, which dominates in $|n=6, k=16\rangle$. The manifold overlapping and crossings in the intermediate regime bring in different state-preparation schemes in addition to the existing ones, e.g., based on adiabatic ramping in the strong interaction regime [67]. The state-preparation scheme in the intermediate regime follows the avoided-crossing-based scenario, which has been widely applied in various setups, such as in Rydberg atoms [87–89].

The formation and avoided crossings of the manifolds in the intermediate regime are common properties of finite spinor lattices and can be generalized to larger systems. Figure 6 presents the related results in the system of $(4\uparrow 4\downarrow 1h)$. In Fig. 6(a), the spectrum as a function of the interaction strength U is shown, where the well-gapped spectrum evolves to gapless from the strong to intermediate interaction regime. The supervised eigenstate categorization in the whole interaction interval indicates that the multimanifold structure is maintained in the intermediate regime, which is indicated by the colors of the eigenenergies in the spectrum. Figure 6(a2) quantifies the ratio of the categorizable eigenstates to the total low-lying eigenstates dominated by the single-occupation states and confirms that most eigenstates in the intermediate regime are categorizable. The overlapping and crossings of different manifolds are then plotted in Figs. 6(b) and 6(c), respectively. Figures 6(b) and 6(c) confirm that the formation of the manifold structure is attributed to the nonvanishing energy spacing due to the finite-size effect, and both the direct and avoided crossings show up; the avoided crossing is associated with the uncategorizable eigenstates.

IV. DISCUSSION AND CONCLUSION

In this work, we numerically investigated the ultracold spinor atoms confined in one-dimensional optical lattices, with a focus on the finite lattice systems in the intermediate interaction regime, which are highly relevant to current experiments. Our investigation revealed the transition from the strong to intermediate regime, in which the eigenenergy spectrum becomes gapless while the eigenstates retain good categorizability into different manifolds. The formation of the manifold structure in the intermediate regime can be attributed to the minigaps between close-lying eigenstates introduced by the finite-size effect, which prevents the intermanifold couplings. The vanishing of the intermanifold gaps leads to

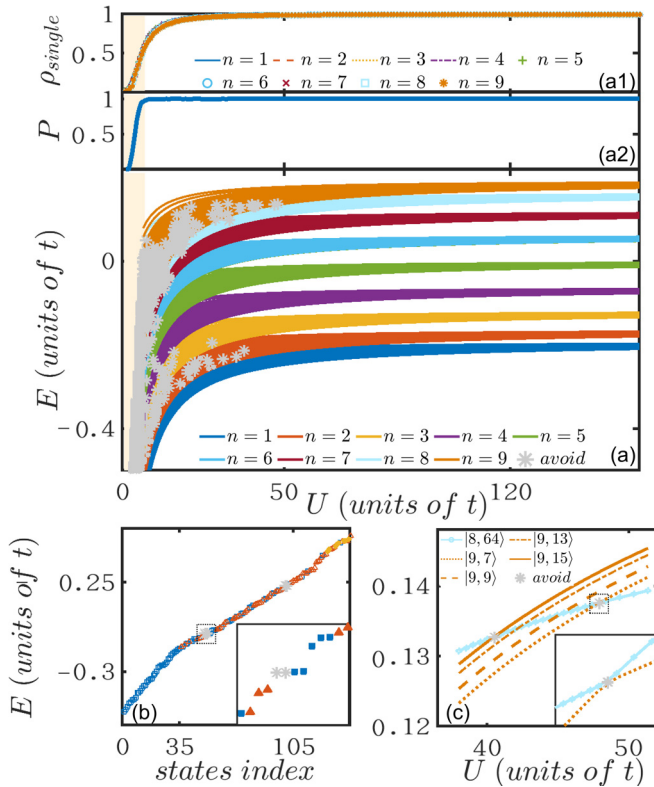


FIG. 6. (a) The eigenenergy spectrum for $(4 \uparrow 4 \downarrow 1h)$. Eigenstates of the same manifold are marked with the same color, and the uncategorized eigenstates are shown with gray stars. (a1) The lowest occupancy probability of the single-occupation basis of the eigenstates in each manifold. (a2) The ratio of categorizable eigenstates to the total low-lying eigenstates in different interaction regimes. (b) Eigenenergy spectrum at $U = 21$; gray stars indicate the uncategorized eigenstates, and the blue squares, red triangles, and yellow dots show the eigenstates of the first, second, and third manifolds, respectively. The inset zooms in on the dashed box regime in the spectrum, around a pair of uncategorized eigenenergies. (c) Eigenenergies as a function of interaction strength for $|n = 9, k = 7, 9, 13, 15\rangle$ and $|n = 8, k = 64\rangle$, with the inset zooming in on the dashed box marked in the main panel

rich direct and avoided crossings between different manifolds. The combined symmetries determine whether the crossing is a direct or avoided one, and the avoided crossing can be explored for state preparations and manipulations, through interaction quench between different avoided crossings.

Our results based on the single-hole filling can be directly generalized to broader systems, e.g., with more hole fillings or under different external potentials. Doping more holes and engineering the external potentials could give rise to manifold structures and crossing behaviors, which could find applications in the state manipulations. Moreover, it also remains an open question whether the categorization in the intermediate interaction regime can be maintained in large systems, e.g., in lattices approaching the thermalization limit, and this could be resolved by methods such as the Bethe ansatz.

In this work, we have explored the well-developed wave-function classification based on supervised machine learning for the categorization of the eigenstates in the intermediate

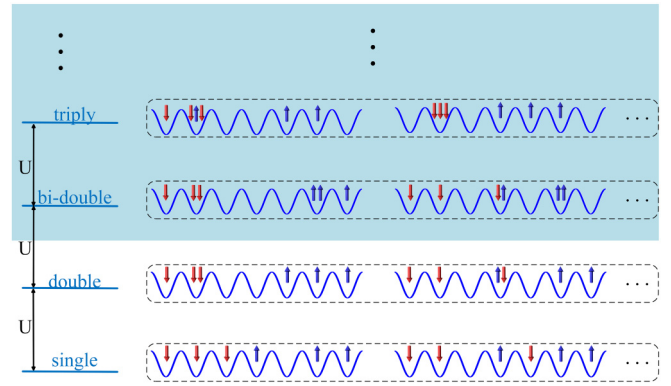


FIG. 7. Schematic representation of the system's single-occupation basis states, double-occupation basis states, and multiple-occupation basis states.

regime. The wave-function classification has been widely applied to the identification of the phase transition [82–84], chaotic behavior [90,91], integrability [92], and so on; our work extends the applicability of this method to identify and categorize eigenstates in the gapless spectrum, which could have applications in a wider range of systems.

ACKNOWLEDGMENTS

The authors would like to acknowledge L. You for inspiring discussions. This work was supported by the National Natural Science Foundation of China (Grants No. 11625417, No. 11604107, No. 91636219, and No. 11727809).

APPENDIX A: DERIVATION AND VALIDITY OF THE EFFECTIVE HAMILTONIAN

In this work, we derived the t - J like Hamiltonian, which can capture the low-lying eigenstates in the intermediate regime. The derivation of the t - J model follows the standard second-order perturbation theory. The perturbation treatment is based on the energetic decoupling of the complete Hamiltonian to various subspaces. Each subspace is composed of basis states of the same chemical potential, and different subspaces are energetically detuned from each other. As sketched in Fig. 7, the single-occupation basis states form a subspace with the lowest chemical potential, and the subspace lying close above constitutes the double-occupation basis states. Above the single- and double-occupation subspaces, there lie subspaces formed by basis states of higher occupations, such as the bidouble-occupation basis and the triple-occupation states. In this work, we focus on the low-lying eigenstates in the intermediate interaction regime, which mainly lie in the single-occupation subspace. Under this condition, we restrict ourselves to a single-occupation subspace and derive an effective Hamiltonian within the single-occupation subspace, which can well reproduce the eigenstates properties of the original Hamiltonian.

The effective Hamiltonian is spanned by the single-occupation basis states, and the higher-occupation states contribute to the higher-order coupling between the single-occupation states. In our derivation, we take into account

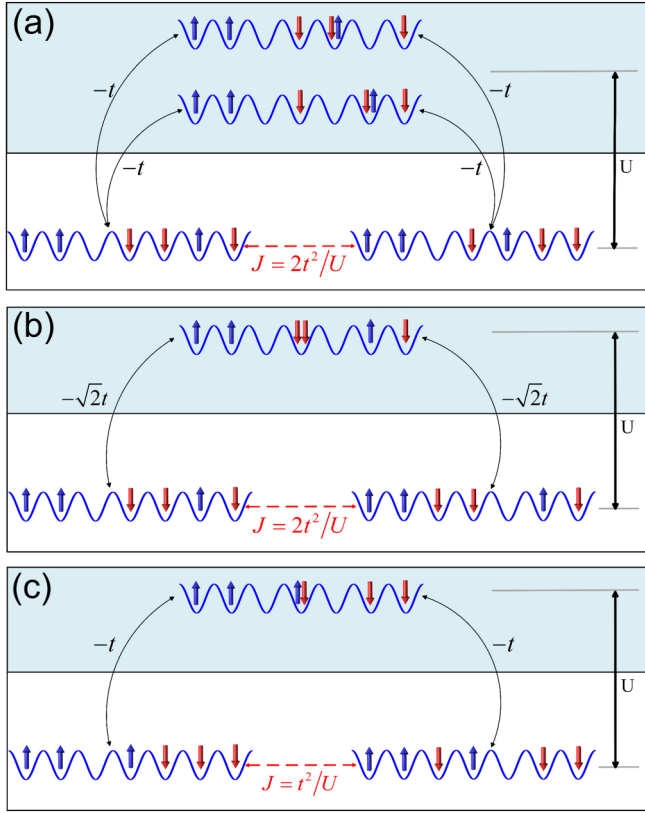


FIG. 8. Three typical pathways of the second-order processes in the perturbation theory. (a) Effective spin-exchange interactions by second-order processes. (b) Spin-preservation interactions with hole next-nearest-neighbor tunneling by second-order processes. (c) Spin-exchange interactions with hole next-nearest-neighbor tunneling by second-order processes.

only the second-order couplings intermediated by the double-occupation states and ignore even higher-order processes. The second-order coupling can be written as

$$H_{m,n}^{\text{eff}} = - \sum_k \langle m | \hat{H}_s | k \rangle \frac{1}{\langle k | \hat{H}_{\text{int}} | k \rangle} \langle k | \hat{H}_s | n \rangle, \quad (\text{A1})$$

where $|m\rangle$ and $|n\rangle$ are single-occupation basis states and $|k\rangle$ is the intermediate double-occupation basis states. In the above equation, \hat{H}_s refers to the first term of H in Eq. (1), i.e., the single-particle tunneling, which couples the single- and double-occupation basis states, and \hat{H}_{int} is the on-site interaction term in Eq. (1). The second-order couplings between the single-occupation basis states are sketched in Fig. 8, where three representative processes are shown. The processes refer to the spin-spin exchange interaction with and without the next-nearest-neighbor hopping of the hole, and the coefficients are different, which is due to the bosonic statistics.

The validity of the effective Hamiltonian can be verified by comparing the eigenenergy and eigenstates obtained with the original and effective Hamiltonians. Figure 9(a) compares the eigenenergies of various eigenstates obtained by the two Hamiltonians, in which we pick one eigenstate from each manifold. It can be shown that in the intermediate and strong interaction regimes, the eigenenergies obtained from the two Hamiltonians match each other very well, and deviations

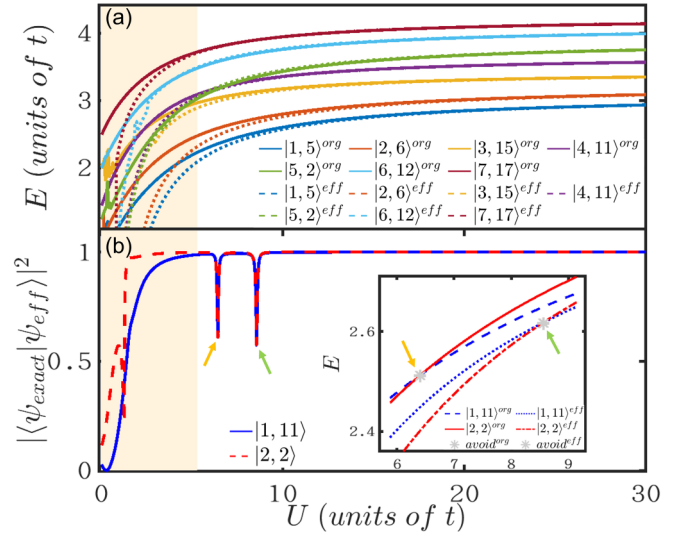


FIG. 9. The comparison between the spectrum in (a) and the overlap of the eigenstates was obtained using the ML-MCTDHX method and the effective t - J model. (a) shows a comparison between the exact spectrum (solid lines) with the effective spectrum (dotted lines). The eigenenergies of the different manifolds are marked with different colored lines. In (b), we present the overlap between the exact and effective eigenstates $|1, 11\rangle$ (solid line) and $|2, 2\rangle$ (dashed line). The inset shows the energy of eigenstates $|1, 11\rangle$ (blue lines) and $|2, 2\rangle$ (red lines) near avoided-crossing points.

mainly emerge in the weak interaction regime. This demonstrates that the effective Hamiltonian can very well reproduce the eigenenergy spectrum in the intermediate regime.

To more strictly ensure the validity of the effective Hamiltonian, we further compare the wave functions of the eigenstates obtained from the original and effective Hamiltonians, as shown in Fig. 9(b). The comparison is done by directly overlapping the eigenstates ${}_{\text{org}}\langle n, k | n, k \rangle_{\text{eff}}$, where $|n, k\rangle_{\text{eff}(\text{org})}$ denotes the k th eigenstate in the n th manifold obtained with the effective (original) Hamiltonian. Figure 9(b) shows that the overlap remains close to unity almost everywhere in the intermediate and strong interaction regimes and decays in the weak interaction regime. This verifies the validity of the effective Hamiltonian. It is noticeable that two dips exist on the overlap curve in the intermediate regime, which illustrates a big mismatch in the related interaction strength. The inset in Fig. 9(b) shows that at the left and right dips, an avoided crossing takes place in the original and effective Hamiltonians, respectively. The mismatch can then be attributed to the fact that the effective Hamiltonian can also reproduce the avoided crossing, but with a relatively small shift in the interaction strength. This could be due to the fact that the effective Hamiltonian takes into account only the second-order perturbation, and the mismatch can be cured by going to even higher-order processes. In general the comparison of the eigenenergy spectrum and the eigenstate wave functions between the effective and the original Hamiltonians verifies that the effective Hamiltonian can very well reproduce the manifold formation and crossings predicted in the original Hamiltonian, with a relatively weak quantitative mismatch.

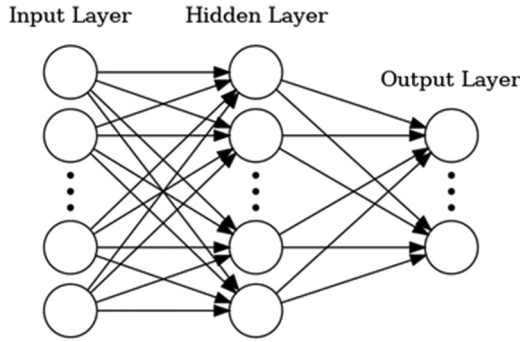


FIG. 10. Illustration of a neural network. The inputs are the complete eigenstates of the system under different interactions, and the outputs are the probability of the eigenstate belonging to one manifold, with each node in the output layer associated to one manifold.

APPENDIX B: MACHINE-LEARNING-BASED APPROACH

We adopt supervised machine learning for the categorization of the low-lying eigenstates in the intermediate regime. The architecture of the neural network employed in our supervised learning is shown in Fig. 10. The network constitutes a single hidden layer of 32 neurons, linking the input and the output layers. The input layer is associated with the wave function of the eigenstates, with each neuron representing one expansion coefficient of the wave function, and the output layer contains neurons with the same number of possible manifolds; the output is the probability of the input eigenstate

TABLE I. Training hyperparameters.

Hyperparameters	Value
Hidden size	32
Activation	[relu, softmax]
Optimizer	Adam
Learning rate	0.001
Decay of momenta	[0.9, 0.999]

belonging to this manifold. The general task of the neuron network is to build the mapping between each eigenstate and the manifold to which the eigenstate should belong.

It is known that the eigenstates in the strong interaction regime can be categorized into different manifolds, and the categorization in the strong interaction regime provides the training samples, in which each eigenstate is labeled with its associated manifold. In our training, we take the eigenstates in the interaction interval $U \in [35, 100]$, with 200 samples in total. The loss function minimized in the training is chosen to be

$$L(f(x), y) = - \sum_i y_i \log_2 [f(x)]_i, \quad (\text{B1})$$

where x and y refer to the input wave function and the output manifold, respectively. The additional hyperparameter is given in Table I.

- [1] Y. Kawaguchi and M. Ueda, *Phys. Rep.* **520**, 253 (2012).
- [2] D. M. Stamper-Kurn and M. Ueda, *Rev. Mod. Phys.* **85**, 1191 (2013).
- [3] J. Stenger, S. Inouye, D. Stamper-Kurn, H.-J. Miesner, A. Chikkatur, and W. Ketterle, *Nature (London)* **396**, 345 (1998).
- [4] C. V. Ciobanu, S.-K. Yip, and T.-L. Ho, *Phys. Rev. A* **61**, 033607 (2000).
- [5] L. Sadler, J. Higbie, S. Leslie, M. Vengalattore, and D. Stamper-Kurn, *Nature (London)* **443**, 312 (2006).
- [6] S. J. Huh, K. Kim, K. Kwon, and J.-Y. Choi, *Phys. Rev. Res.* **2**, 033471 (2020).
- [7] M. Greiner, O. Mandel, T. Esslinger, T. W. Hänsch, and I. Bloch, *Nature (London)* **415**, 39 (2002).
- [8] M. W. Zwierlein, C. H. Schunck, A. Schirotzek, and W. Ketterle, *Nature (London)* **442**, 54 (2006).
- [9] N. Roch, S. Florens, V. Bouchiat, W. Wernsdorfer, and F. Balestro, *Nature (London)* **453**, 633 (2008).
- [10] N. Gemelke, X. Zhang, C.-L. Hung, and C. Chin, *Nature (London)* **460**, 995 (2009).
- [11] P. A. Murthy, I. Boettcher, L. Bayha, M. Holzmann, D. Kedar, M. Neidig, M. G. Ries, A. N. Wenz, G. Zürn, and S. Jochim, *Phys. Rev. Lett.* **115**, 010401 (2015).
- [12] L. A. Williamson and P. B. Blakie, *Phys. Rev. Lett.* **116**, 025301 (2016).
- [13] L. A. Williamson and P. B. Blakie, *Phys. Rev. Lett.* **119**, 255301 (2017).
- [14] K. Fujimoto, R. Hamazaki, and M. Ueda, *Phys. Rev. Lett.* **120**, 073002 (2018).
- [15] S.-F. Guo, F. Chen, Q. Liu, M. Xue, J.-J. Chen, J.-H. Cao, T.-W. Mao, M. K. Tey, and L. You, *Phys. Rev. Lett.* **126**, 060401 (2021).
- [16] H. Flayac, I. A. Shelykh, D. D. Solnyshkov, and G. Malpuech, *Phys. Rev. B* **81**, 045318 (2010).
- [17] T. W. A. Montgomery, W. Li, and T. M. Fromhold, *Phys. Rev. Lett.* **111**, 105302 (2013).
- [18] M. Ueda, *Rep. Prog. Phys.* **77**, 122401 (2014).
- [19] J. Ruostekoski and J. R. Anglin, *Phys. Rev. Lett.* **91**, 190402 (2003).
- [20] V. Pietilä and M. Möttönen, *Phys. Rev. Lett.* **103**, 030401 (2009).
- [21] M. Ray, E. Ruokokoski, K. Tiurev, M. Möttönen, and D. Hall, *Science* **348**, 544 (2015).
- [22] M. A. Cazalilla, A. Ho, and M. Ueda, *New J. Phys.* **11**, 103033 (2009).
- [23] A. V. Gorshkov, M. Hermele, V. Gurarie, C. Xu, P. S. Julienne, J. Ye, P. Zoller, E. Demler, M. D. Lukin, and A. Rey, *Nat. Phys.* **6**, 289 (2010).
- [24] L. Messio and F. Mila, *Phys. Rev. Lett.* **109**, 205306 (2012).
- [25] X. Zhang, M. Bishof, S. L. Bromley, C. V. Kraus, M. S. Safronova, P. Zoller, A. M. Rey, and J. Ye, *Science* **345**, 1467 (2014).
- [26] B. Yang, H. Sun, R. Ott, H.-Y. Wang, T. V. Zache, J. C. Halimeh, Z.-S. Yuan, P. Hauke, and J.-W. Pan, *Nature (London)* **587**, 392 (2020).
- [27] B. Yang, H. Sun, C.-J. Huang, H.-Y. Wang, Y. Deng, H.-N. Dai, Z.-S. Yuan, and J.-W. Pan, *Science* **369**, 550 (2020).

- [28] H.-N. Dai, B. Yang, A. Reingruber, H. Sun, X.-F. Xu, Y.-A. Chen, Z.-S. Yuan, and J.-W. Pan, *Nat. Phys.* **13**, 1195 (2017).
- [29] H. Sun, B. Yang, H.-Y. Wang, Z.-Y. Zhou, G.-X. Su, H.-N. Dai, Z.-S. Yuan, and J.-W. Pan, *Nat. Phys.* **17**, 990 (2021).
- [30] X.-Y. Luo, Y.-Q. Zou, L.-N. Wu, Q. Liu, M.-F. Han, M. K. Tey, and L. You, *Science* **355**, 620 (2017).
- [31] Y.-Q. Zou, L.-N. Wu, Q. Liu, X.-Y. Luo, S.-F. Guo, J.-H. Cao, M. K. Tey, and L. You, *Proc. Natl. Acad. Sci. USA* **115**, 6381 (2018).
- [32] Q. Liu, L.-N. Wu, J.-H. Cao, T.-W. Mao, X.-W. Li, S.-F. Guo, M. K. Tey, and L. You, *Nat. Phys.* **18**, 167 (2022).
- [33] L. Pezze, A. Smerzi, M. K. Oberthaler, R. Schmied, and P. Treutlein, *Rev. Mod. Phys.* **90**, 035005 (2018).
- [34] C. Gross, T. Zibold, E. Nicklas, J. Esteve, and M. K. Oberthaler, *Nature (London)* **464**, 1165 (2010).
- [35] M. Kitagawa and M. Ueda, *Phys. Rev. A* **47**, 5138 (1993).
- [36] J. Ma, X. Wang, C. Sun, and F. Nori, *Phys. Rep.* **509**, 89 (2011).
- [37] O. Hosten, R. Krishnakumar, N. J. Engelsen, and M. A. Kasevich, *Science* **352**, 1552 (2016).
- [38] S. Yi, Ö. E. Müstecaplıoğlu, C.-P. Sun, and L. You, *Phys. Rev. A* **66**, 011601(R) (2002).
- [39] M. Koashi and M. Ueda, *Phys. Rev. Lett.* **84**, 1066 (2000).
- [40] S. Yi, L. You, and H. Pu, *Phys. Rev. Lett.* **93**, 040403 (2004).
- [41] T. Ohmi and K. Machida, *J. Phys. Soc. Jpn.* **67**, 1822 (1998).
- [42] H. Pu, C. K. Law, S. Raghavan, J. H. Eberly, and N. P. Bigelow, *Phys. Rev. A* **60**, 1463 (1999).
- [43] T.-L. Ho, *Phys. Rev. Lett.* **81**, 742 (1998).
- [44] P. Xu, S. Yi, and W. Zhang, *Phys. Rev. Lett.* **123**, 073001 (2019).
- [45] L. Chang, Q. Zhai, R. Lu, and L. You, *Phys. Rev. Lett.* **99**, 080402 (2007).
- [46] B. Evrard, A. Qu, J. Dalibard, and F. Gerbier, *Science* **373**, 1340 (2021).
- [47] B. Evrard, A. Qu, J. Dalibard, and F. Gerbier, *Phys. Rev. Lett.* **126**, 063401 (2021).
- [48] Q. Guan, G. W. Biedermann, A. Schwettmann, and R. J. Lewis-Swan, *Phys. Rev. A* **104**, 042415 (2021).
- [49] A. E. Leanhardt, Y. Shin, D. Kielpinski, D. E. Pritchard, and W. Ketterle, *Phys. Rev. Lett.* **90**, 140403 (2003).
- [50] S. Yi and H. Pu, *Phys. Rev. Lett.* **97**, 020401 (2006).
- [51] L. Santos, G. V. Shlyapnikov, and M. Lewenstein, *Phys. Rev. Lett.* **90**, 250403 (2003).
- [52] H. Pu, S. Raghavan, and N. P. Bigelow, *Phys. Rev. A* **61**, 023602 (2000).
- [53] M.-S. Chang, Q. Qin, W. Zhang, L. You, and M. S. Chapman, *Nat. Phys.* **1**, 111 (2005).
- [54] J. Jie, Q. Guan, S. Zhong, A. Schwettmann, and D. Blume, *Phys. Rev. A* **102**, 023324 (2020).
- [55] T. Kinoshita, T. Wenger, and D. S. Weiss, *Science* **305**, 1125 (2004).
- [56] S. Palzer, C. Zipkes, C. Sias, and M. Köhl, *Phys. Rev. Lett.* **103**, 150601 (2009).
- [57] B. Paredes, A. Widera, V. Murg, O. Mandel, S. Fölling, I. Cirac, G. V. Shlyapnikov, T. W. Hänsch, and I. Bloch, *Nature (London)* **429**, 277 (2004).
- [58] P. Vignolo and A. Minguzzi, *Phys. Rev. Lett.* **110**, 020403 (2013).
- [59] F. Deuretzbacher, D. Becker, J. Bjerlin, S. M. Reimann, and L. Santos, *Phys. Rev. A* **90**, 013611 (2014).
- [60] A. Volosniev, D. V. Fedorov, A. S. Jensen, M. Valiente, and N. T. Zinner, *Nat. Commun.* **5**, 5300 (2014).
- [61] J. Levensen, P. Massignan, G. M. Bruun, and M. M. Parish, *Sci. Adv.* **1**, e1500197 (2015).
- [62] P. Massignan, J. Levensen, and M. M. Parish, *Phys. Rev. Lett.* **115**, 247202 (2015).
- [63] A. G. Volosniev, D. Petrosyan, M. Valiente, D. V. Fedorov, A. S. Jensen, and N. T. Zinner, *Phys. Rev. A* **91**, 023620 (2015).
- [64] O. V. Marchukov, A. G. Volosniev, M. Valiente, D. Petrosyan, and N. Zinner, *Nat. Commun.* **7**, 13070 (2016).
- [65] L. Yang, L. Guan, and H. Pu, *Phys. Rev. A* **91**, 043634 (2015).
- [66] L. Yang and H. Pu, *Phys. Rev. A* **94**, 033614 (2016).
- [67] R. E. Barfknecht, A. Foerster, and N. T. Zinner, *Phys. Rev. A* **95**, 023612 (2017).
- [68] F. Deuretzbacher, D. Becker, J. Bjerlin, S. M. Reimann, and L. Santos, *Phys. Rev. A* **95**, 043630 (2017).
- [69] S. S. Alam, T. Skaras, L. Yang, and H. Pu, *Phys. Rev. Lett.* **127**, 023002 (2021).
- [70] L. Yang and X. Cui, *Phys. Rev. A* **93**, 013617 (2016).
- [71] H. H. Jen and S.-K. Yip, *Phys. Rev. A* **95**, 053631 (2017).
- [72] Y. Liu, S. Chen, and Y. Zhang, *Phys. Rev. A* **95**, 043628 (2017).
- [73] S. Krönke, L. Cao, O. Vendrell, and P. Schmelcher, *New J. Phys.* **15**, 063018 (2013).
- [74] L. Cao, S. Krönke, O. Vendrell, and P. Schmelcher, *J. Chem. Phys.* **139**, 134103 (2013).
- [75] L. Cao, V. Bolsinger, S. Mistakidis, G. Koutentakis, S. Krönke, J. Schurer, and P. Schmelcher, *J. Chem. Phys.* **147**, 044106 (2017).
- [76] J. Vijayan, P. Sompet, G. Salomon, J. Koepsell, S. Hirthe, A. Bohrdt, F. Grusdt, I. Bloch, and C. Gross, *Science* **367**, 186 (2020).
- [77] T. A. Hilker, G. Salomon, F. Grusdt, A. Omran, M. Boll, E. Demler, I. Bloch, and C. Gross, *Science* **357**, 484 (2017).
- [78] V. J. Emery, S. A. Kivelson, and H. Q. Lin, *Phys. Rev. Lett.* **64**, 475 (1990).
- [79] M. Ogata, M. U. Luchini, S. Sorella, and F. F. Assaad, *Phys. Rev. Lett.* **66**, 2388 (1991).
- [80] F. Grusdt, A. Bohrdt, and E. Demler, *Phys. Rev. B* **99**, 224422 (2019).
- [81] F. Grusdt and L. Pollet, *Phys. Rev. Lett.* **125**, 256401 (2020).
- [82] J. Carrasquilla and R. G. Melko, *Nat. Phys.* **13**, 431 (2017).
- [83] E. P. Van Nieuwenburg, Y.-H. Liu, and S. D. Huber, *Nat. Phys.* **13**, 435 (2017).
- [84] K. Ch'ng, J. Carrasquilla, R. G. Melko, and E. Khatami, *Phys. Rev. X* **7**, 031038 (2017).
- [85] M. Innes, E. Saba, K. Fischer, D. Gandhi, M. C. Rudilosso, N. M. Joy, T. Karmali, A. Pal, and V. Shah, arXiv:1811.01457.
- [86] M. Innes, *J. Open Source Software* **3**, 602 (2018).
- [87] M. Kurz and P. Schmelcher, *Phys. Rev. A* **88**, 022501 (2013).
- [88] M. Kurz and P. Schmelcher, *J. Phys. B* **47**, 165101 (2014).
- [89] A. Gaj, A. T. Krupp, P. Ilzhöfer, R. Löw, S. Hofferberth, and T. Pfau, *Phys. Rev. Lett.* **115**, 023001 (2015).
- [90] D. W. Alves and M. O. Flynn, *Phys. Rev. A* **101**, 052338 (2020).
- [91] Y. A. Kharkov, V. E. Sotskov, A. A. Karazeev, E. O. Kiktenko, and A. K. Fedorov, *Phys. Rev. B* **101**, 064406 (2020).
- [92] S. Krippendorf, D. Lüst, and M. Syvaeri, *Fortschr. Phys.* **69**, 2100057 (2021).